INTERNATIONAL JOURNAL FOR NUMERICAL METHODS IN FLUIDS, VOL. 26, 323–343 (1998)

COMPUTATION OF BUOYANCY-DRIVEN FLOW IN AN ECCENTRIC CENTRIFUGAL ANNULUS WITH A NON-ORTHOGONAL COLLOCATED FINITE VOLUME ALGORITHM

MING-I CHAR* AND YUAN-HSIUNG HSU

Department of Applied Mathematics, National Chung Hsing University, Taichung 40227, Taiwan, Republic of China

SUMMARY

A computational study is performed on two-dimensional mixed convection in an annulus between a horizontal outer cylinder and a heated, rotating, eccentric inner cylinder. The computation has been done using a non-orthogonal grid and a fully collocated finite volume procedure. Solutions are iterated to convergence through a pressure correction scheme and the convection is treated by Van Leer's MUSCL scheme. The numerical procedure adopted here can easily eliminate the 'Numerical leakage' phenomenon of the mixed convection problem whereby strong buoyancy and centrifugal effects are encountered in the case of a highly eccentric annulus. Numerical results have been obtained for Rayleigh number Ra ranging from 7×10^3 to 10^7, Reynolds number Re from 0 to 1200 and Prandtl number Pr from 0.01 to 7. The mixed rotation parameter σ ($= Ra/PrRe^2$) varies from ∞ (pure natural convection) to 0.01 with various eccentricities ε. The computational results are in good agreement with previous works which show that the mixed convection heat transfer characteristics in the annulus are significantly affected by σ and ε. The results indicate that the mean Nusselt number $\overline{Nu}$ increases with increasing Ra or Pr but decreases with increasing Re. In the case of a highly eccentric annulus the conduction effect becomes predominant in the throat gap. Hence the crucial phenomenon on whereby $\overline{Nu}$ first decreases and then increases can be found with increasing eccentricity. © 1998 John Wiley & Sons, Ltd.

Int. J. Numer. Meth. Fluids **26**: 323–343 (1998)

KEY WORDS: mixed convection; finite volume algorithm; eccentricity; Nusselt number

1. INTRODUCTION

The problem of mixed convection flow in a rotating system has received considerable attention recently because of its numerous applications. Such applications are encountered in seeking improvements for crystallographic perfection in industrial processing [1,2], food processing [3], heat removal from nuclear reactor fuel rods, double-pipe heat exchangers and underground electric transmission cables using pressurized gas. Quite often the eccentricity results from high angular velocity of the blade or shaft in the rotating machinery or from manufacturing tolerance or thermal deformation in a device of nominally concentric annulus. In this case the effect of eccentricity on the convection heat transfer in the annulus becomes inevitable.

Owing to the viscous shearing effects at the end walls, a three-dimensional analysis of mixed convection flow is necessary when the annulus has a finite length. However, with a sufficiently

* Correspondence to: Department of Applied Mathematics, National Chung Hsing University, Taichung 40227, Taiwan, Republic of China.

CCC 0271–2091/98/030323–21$17.50

Received August 1995
Revised April 1996

long annulus, Desai and Vafai [4] showed that there exists a core region, over a substantial length of the cavity, which can be approximated by a two-dimensional model. Most heat transfer studies on two-dimensional eccentric annuli have been concerned with either pure free convection [5,6] or pure forced convection [7,8]. Only a few researchers have addressed the problem of laminar mixed convection in a horizontal eccentric annulus with a heated rotating inner cylinder even though it occurs in most engineering applications. Lee [9] studied the effect of convective fluid motion of air enclosed in an annulus between two eccentric cylinders with a heated horizontal rotating inner cylinder. He obtained numerical results for $Pr = 0.7$, with Re ranging from 0 to 1120, Ra from 10^4 to 10^5 and ε from $-2/3$ to $2/3$.

More recently, Choudhury and Karki [10] considered laminar mixed convection in a horizontal eccentric annulus. The values of eccentricity ε considered were in the range from 0 to 0.6. Their numerical results showed that the eccentricity introduces additional non-uniformity in the flow and temperature fields. Some studies were performed by Gardiner and Sabersky [11] on concentric cylinders with three different Prandtl numbers, namely 2.5, 4.5 and 6.5. Experimental analysis of the thermal fields in horizontal eccentric cylindrical annuli was undertaken by Guj *et al.* [12].

Most heat transfer studies on the laminar mixed convection problem have been carried out using a staggered grid arrangement and a streamfunction–vorticity formulation, [9,13] vorticity–velocity formulation [14] or primitive variable formulation [15] based on the finite difference method. These studies indicated that in the mixed convection problem with a strong convective influence or a highly eccentric cylindrical annulus 'numerical leakage' occurs around the inner cylinder. Now a numerical procedure employing a non-orthogonal mesh which has a fully collocated storage arrangement for all variables in a finite volume formulation is used for studying the strong convective phenomenon in a highly eccentric annulus. This numerical procedure can easily eliminate the chequerboard oscillation found under strong rotation in a highly eccentric annulus.

The interaction of the buoyancy- and centrifugally driven fluid with the effect of strong rotation ($Re \geq 2000$) produces a complex three-dimensional flow with Taylor vortices [8] in the eccentric annulus. The present work limits the numerical studies to a range of rotational parameters ($Re \leq 1200$) before the three-dimensional effects set in. The purpose of this study is to find the optimal location where the minimum heat transfer occurs. The results presented here cover a range of Rayleigh number Ra, Reynolds number Re, Prandtl number Pr and mixed rotational parameter σ for various eccentricities ε. Their effects on the fluid flow and heat transfer characteristics are discussed. Finally, correlation equations for the mean Nusselt number $\overline{Nu}$ are also presented.

2. MATHEMATICAL FORMULATION

2.1. Governing equations

The present paper studies the problem of laminar mixed convection flow in an annulus between two eccentric horizontal cylinders, the inner one of which is heated and rotating. A schematic diagram of the physical model and co-ordinate system is shown in Figure 1. The inner cylinder is heated and rotates in the counterclockwise direction. The eccentricity e is defined as the offset between the two cylinder centres and the eccentricity configuration is aligned with the gravity vector. It is assumed that the flow in the annular region is steady, incompressible, laminar without Taylor vortices ($Re \leq 1200$). The annulus has infinite length

and the thermophysical properties of the fluid are assumed constant except for the density in the buoyancy term in the momentum equation. Therefore the two-dimensional model and the Boussinesq approximation are applicable.

Under the foregoing assumptions the governing equations for the conservation of mass, momentum and energy in Cartesian co-ordinates for the problem of mixed convection in an eccentric cylinder annulus can be written as

$$\frac{\partial u}{\partial x}+\frac{\partial v}{\partial y}=0, \tag{1}$$

$$u\frac{\partial u}{\partial x}+v\frac{\partial u}{\partial y}=-\frac{1}{\rho}\frac{\partial p}{\partial x}+\nu\left(\frac{\partial^2 u}{\partial x^2}+\frac{\partial^2 u}{\partial y^2}\right), \tag{2}$$

$$u\frac{\partial v}{\partial x}+v\frac{\partial v}{\partial y}=-\frac{1}{\rho}\frac{\partial p}{\partial y}+\nu\left(\frac{\partial^2 v}{\partial x^2}+\frac{\partial^2 v}{\partial y^2}\right)+g\beta(T-T_{\mathrm{o}}), \tag{3}$$

$$u\frac{\partial T}{\partial x}+v\frac{\partial T}{\partial y}=\alpha\left(\frac{\partial^2 T}{\partial x^2}+\frac{\partial^2 T}{\partial y^2}\right). \tag{4}$$

It may be noted that even though this is a cylindrical system problem, owing to the eccentric annulus, the outer cylinder boundary and the generation of computational grids are difficult to describe with cylindrical co-ordinates. Moreover, the system of governing equations is solved by the finite volume method in the current study. The advantage of this method is that it allows one to deal with complicated geometries without considering the equations written in cylindrical co-ordinates. Hence Cartesian co-ordinates were used here to formulate the problem. We now introduce the dimensionless variables

$$X=\frac{x}{L},\qquad Y=\frac{y}{L},\qquad U=\frac{u}{R_{\mathrm{i}}\omega},\qquad V=\frac{v}{R_{\mathrm{i}}\omega},\qquad P=\frac{p}{\rho R_{\mathrm{i}}^2\omega^2},\qquad \Theta=\frac{T-T_{\mathrm{o}}}{T_{\mathrm{i}}-T_{\mathrm{o}}}, \tag{5}$$

where L is the characteristic length ($L=R_{\mathrm{o}}-R_{\mathrm{i}}$) and ω is the rotational speed of the inner cylinder. The governing equations can be written in dimensionless form as

$$\frac{\partial U}{\partial X}+\frac{\partial V}{\partial Y}=0, \tag{6}$$

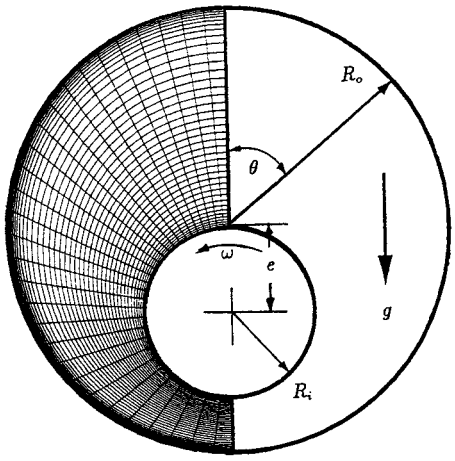

Figure 1. Physical model and computational grid

$$U\frac{\partial U}{\partial X}+V\frac{\partial U}{\partial Y}=-\frac{\partial P}{\partial X}+\frac{1}{Re}\left(\frac{\partial^2 U}{\partial X^2}+\frac{\partial^2 U}{\partial Y^2}\right), \tag{7}$$

$$U\frac{\partial V}{\partial X}+V\frac{\partial V}{\partial Y}=-\frac{\partial P}{\partial Y}+\frac{1}{Re}\left(\frac{\partial^2 V}{\partial X^2}+\frac{\partial^2 V}{\partial Y^2}\right)+\frac{Ra}{Pr\,Re^2}\Theta, \tag{8}$$

$$U\frac{\partial \Theta}{\partial X}+V\frac{\partial \Theta}{\partial y}=\frac{1}{Pr\,Re}\left(\frac{\partial^2 \Theta}{\partial X^2}+\frac{\partial^2 \Theta}{\partial Y^2}\right), \tag{9}$$

where $Re=R_i\omega L/v$ is the Reynolds number, $Ra=g\beta L^3 T_m/v\alpha$ is the Rayleigh number, $T_m=T_i-T_o$ is the maximum temperature difference and $Pr=v/\alpha$ is the Prandtl number.

The boundary conditions for this problem with the heated inner cylinder rotating at an angular velocity ω can be written using no-slip conditions of the velocity at the boundary, uniform but different temperatures of the inner and outer cylinders and vanishing of the pressure gradient on the boundary. Thus the dimensionless boundary conditions are

$$U=-\cos\theta,\quad V=\sin\theta,\quad \frac{\partial P}{\partial n}=0,\quad \Theta=1\quad \text{at } \bar{R}=1\ (R=R_i),\quad 0\le\theta\le 2\pi, \tag{10}$$

$$U=0,\quad V=0,\quad \frac{\partial P}{\partial n}=0,\quad \Theta=0\quad \text{at } \bar{R}=RR\ (R=R_o),\quad 0\le\theta\le 2\pi, \tag{11}$$

where $\bar{R}=R/R_i$.

2.2. Governing parameters

The governing Equations (6)–(9) contain three independent parameters, namely *Re*, *Ra* and *Pr*. The geometric parameter of eccentricity ε and the mixed rotation parameter σ are given as

$$\varepsilon=\frac{e}{R_o-R_i}, \tag{12}$$

$$\sigma=\frac{Ra}{Pr\,Re^2}. \tag{13}$$

The current study is conducted over a range of *Ra*, *Re* and *Pr*. Seven eccentricities ($\varepsilon=$ 0.8, 0.4, 0.2, 0, -0.2, -0.4, -0.8) and various σ ranging from ∞ (pure natural convection) to 0.01 are considered in the present investigation.

3. NUMERICAL PROCEDURE

3.1. Basic numerical framework

Calculations have been performed with the general non-orthogonal, fully collocated finite volume approach STREAM [16]. The governing equations and boundary conditions in Cartesian co-ordinates (X, Y) will now be transformed into computational co-ordinates (ξ, η) which express the variation in flow properties in curvilinear co-ordinates. In terms of the transformed co-ordinates the governing Equations (6)–(9) become

$$\frac{\partial \bar{U}}{\partial \xi}+\frac{\partial \bar{V}}{\partial \eta}=0, \tag{14}$$

$$\frac{\partial}{\partial\xi}\left(\bar{U}U-\frac{1}{Re}J(q_{11}U_\xi)\right)+\frac{\partial}{\partial\eta}\left(\bar{V}U-\frac{1}{Re}J(q_{22}U_\eta)\right)$$
$$=-(P_\xi Y_\eta-P_\eta Y_\xi)+\frac{1}{Re}\left(\frac{\partial}{\partial\xi}[J(q_{12}U_\eta)]+\frac{\partial}{\partial\eta}[J(q_{12}U_\xi)]\right), \tag{15}$$

$$\frac{\partial}{\partial\xi}\left(\bar{U}V-\frac{1}{Re}J(q_{11}V_\xi)\right)+\frac{\partial}{\partial\eta}\left(\bar{V}V-\frac{1}{Re}J(q_{22}V_\eta)\right)$$
$$=-(P_\eta X_\xi-P_\xi X_\eta)+\frac{Ra}{Pr\,Re^2}\Theta+\frac{1}{Re}\left(\frac{\partial}{\partial\xi}[J(q_{12}V_\eta)]+\frac{\partial}{\partial\eta}[J(q_{12}V_\xi)]\right), \tag{16}$$

$$\frac{\partial}{\partial\xi}\left(\bar{U}\Theta-\frac{1}{Pr\,Re}J(q_{11}\Theta_\xi)\right)+\frac{\partial}{\partial\eta}\left(\bar{V}\Theta-\frac{1}{Pr\,Re}J(q_{22}\Theta_\eta)\right)$$
$$=\frac{1}{Pr\,Re}\left(\frac{\partial}{\partial\xi}[J(q_{12}\Theta_\eta)]+\frac{\partial}{\partial\eta}[J(q_{12}\Theta_\xi)]\right), \tag{17}$$

where $\bar{U}$ and $\bar{V}$ are contravariant velocity components given by

$$\bar{U}=UX_\eta-VY_\eta,\qquad \bar{V}=-UY_\xi+VX_\xi, \tag{18}$$

J is the Jacobian of the transformation defined by

$$J=X_\xi Y_\eta-X_\eta Y_\xi, \tag{19}$$

the subscripts ξ and η denote partial differentiation with respect to their corresponding directions and the coefficients q_{11}, q_{12} and q_{22} are defined as

$$q_{11}=\frac{X_\xi X_\xi+Y_\xi Y_\xi}{J^2},\qquad q_{12}=\frac{X_\xi X_\eta+Y_\xi Y_\eta}{J^2},\qquad q_{22}=\frac{X_\eta X_\eta+Y_\eta Y_\eta}{J^2}. \tag{20}$$

The transformed boundary conditions are

$$U=-\cos\theta,\quad V=\sin\theta,\quad \nabla P=0,\quad \Theta=1\quad \text{at } \eta_{\min}=0, \tag{21}$$

$$U=0,\quad V=0,\quad \nabla P=0,\quad \Theta=0\quad \text{at } \eta_{\max}=1. \tag{22}$$

3.2. Finite volume approximation

The non-orthogonal, fully collocated scheme used in this study is based on a finite volume approximation [17,18]. In a non-orthogonal co-ordinate system the transport Equations (15)–(17) are integrated over the control volume surrounding each interior node of the mesh shown in Figure 2(a) to yield, after application of the Gauss divergence theorem in conjunction with central differencing for diffusion, a balance of face fluxes and volume-integrated net source. The discretized equation can be expressed in the general form

$$\begin{aligned}\bar{U}_e\phi_e-\bar{U}_w\phi_w+\bar{U}_n\phi_n-\bar{U}_s\phi_s=&[(\Gamma_\phi Jq_{11})_e+(\Gamma_\phi Jq_{11})_w+(\Gamma_\phi Jq_{22})_n+(\Gamma_\phi Jq_{22})_s]\phi_P\\&-(\Gamma_\phi Jq_{11})_e\phi_E-(\Gamma_\phi Jq_{11})_w\phi_W-(\Gamma_\phi Jq_{22})_n\phi_N\\&-(\Gamma_\phi Jq_{22})_s\phi_S+J(S^{CD}+S_\phi),\end{aligned} \tag{23}$$

where Γ_ϕ and S_ϕ represent the diffusivity and additional source pertaining to ϕ respectively and ϕ stands for U, V, P or Θ. JS^{CD} is a 'cross-diffusion' term given by

$$JS^{CD}=\frac{\partial}{\partial\xi}\left(\frac{1}{Re}(Jq_{12}\phi_\eta)\right)+\frac{\partial}{\partial\eta}\left(\frac{1}{Re}(Jq_{12}\phi_\xi)\right). \tag{24}$$

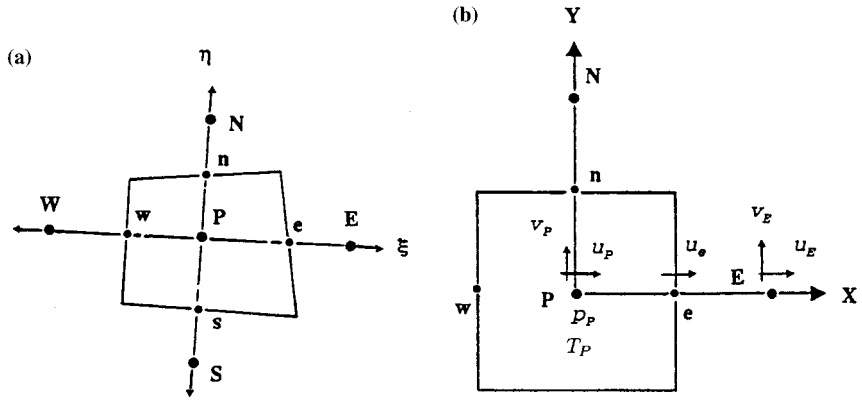

Figure 2. (a) Co-ordinate transformation; (b) finite volume and storage arrangement

The face values of ϕ, i.e. ϕ_e, ϕ_w, etc., are approximated by a first-order upwind scheme. All the sources, including S^{CD} and S_ϕ, are discretized via single-point quadrature, i.e. the volume-averaged source is assumed to be the value residing at the cell-centred node. All cell corner values involved in the cross-diffusion are evaluated by bilinear interpolation. To promote numerical stability via diagonal dominance, the sources are represented in the linearized form

$$J(S^{CD} + S_\phi) = S_P\phi_P + S_C, \tag{25}$$

where S_P and S_C represent the implicit and explicit parts of the source term respectively, with S_P being chosen so that it is unconditionally negative. Substitution of the above expressions into the volume-integrated equation leads to

$$A_P\phi_P = \sum_{m=E,W,N,S} A_m\phi_m + S_\phi, \tag{26}$$

where

$$\begin{aligned} A_E &= (\Gamma_\phi Jq_{11})_e + \langle -\bar{U}_e, 0\rangle, \qquad A_W = (\Gamma_\phi Jq_{11})_w + \langle -\bar{U}_w, 0\rangle, \\ A_N &= (\Gamma_\phi Jq_{22})_n + \langle -\bar{U}_n, 0\rangle, \qquad A_S = (\Gamma_\phi Jq_{22})_s + \langle -\bar{U}_s, 0\rangle, \\ A_P &= A_E + A_W + A_N + A_S - S_P, \end{aligned} \tag{27}$$

in which the symbol $\langle\ \rangle$ denotes the largest of the quantities contained within it. In the above, face diffusivities are evaluated by linear interpolation using neighbouring nodes on either side of any face being considered.

The velocity vector is decomposed into Cartesian components and the convective terms are approximated by van Leer's MUSCL scheme [19]. All dependent variables such as velocity components, pressure and temperature are stored together at the centre of a control volume as shown in Figure 2(b). Such a non-staggered grid arrangement will generally lead to a chequerboard oscillation when pressure gradients are approximated by central differencing, reflecting a computational decoupling of velocity and pressure gradient. To remedy this problem, the method of Rhie and Chow [20] was used. The pressure field is calculated using the SIMPLE algorithm developed by Patankar [21]. The discretized equations are handled successively, the coupling between equations through the source terms being solved iteratively.

The following convergence criterion based on the residue-value (R_u) concept was used:

$$R_{u,\phi} = \sum_{n=1}^{Z} \left(S_\phi - \sum_{m=E,W,P,N,S} A_m^n \phi_m^n \right), \tag{28}$$

$$\mathrm{Max}(R_{u,\phi}) \leq 10^{-5}, \tag{29}$$

where ϕ represents U, V, P or Θ and Z is the number of grid cells.

3.3. Calculation of Nu and $\overline{Nu}$

When the convergence criterion is reached, the local and mean Nusselt numbers on the cylinder wall are calculated. The local Nusselt number on the cylinder wall is defined by

$$Nu_i = -\left(R \frac{\partial \Theta}{\partial R} \right)_{R=R_i} = -\left(\frac{q_{11}\Theta_\eta q_{12}\Theta_\xi}{\sqrt{q_{11}}} \right)_{\eta=\eta_{\min}}, \tag{30}$$

$$Nu_o = -\left(R \frac{\partial \Theta}{\partial R} \right)_{R=R_o} = -\left(\frac{q_{11}\Theta_\eta q_{12}\Theta_\xi}{\sqrt{q_{11}}} \right)_{\eta=\eta_{\max}}. \tag{31}$$

The mean Nusselt number is determined from

$$\overline{Nu}_i = \frac{1}{2\pi} \int_0^{2\pi} Nu_i \, d\theta, \tag{32}$$

$$\overline{Nu}_o = \frac{1}{2\pi} \int_0^{2\pi} Nu_o \, d\theta, \tag{33}$$

$$\overline{Nu} = \frac{1}{2}(\overline{Nu}_i + \overline{Nu}_o). \tag{34}$$

4. RESULTS AND DISCUSSION

In the present work, detailed parametric studies are conducted using a two-dimensional model based on the assumption that the annulus is long enough for axial effects to be neglected. From the foregoing mathematical formulation it can be seen that the dimensionless parameters include Re, Ra, ε and Pr. In the present study, ranges of values of Re (0–1200), Ra (7×10^3–10^7), ε (-0.8 to 0.8), σ (0.01–∞) and Pr (0.01–7) at a fixed radius ratio $RR = 2.6$ are considered. These values were chosen so as to facilitate comparisons with published experimental and numerical data. The majority of numerical results presented here are firstly displayed through streamlines and isotherms. The local and mean heat transfer results are then given by plots showing the Nusselt number variation with the angular position along the inner and outer cylinders for discussion of the interaction between fluid flow and heat transfer.

To examine the grid independence, computations of mean Nusselt number in a concentric rotational annulus with $RR = 2.6$, $Pr = 0.7$, $Ra = 10^6$ and $Re = 1000$ are carried out using four different mesh sizes, namely 41×31, 61×31, 81×41 and 91×61. The results are listed in Table I. It is seen that the maximum difference in mean Nusselt number is approximately 1%, indicating that the results are insensitive to the grid size. Because of the large gradients occurring near the inner and outer walls, the node spacing in the radial direction near the walls is reduced by a factor of two compared with the central region. In the present study a non-uniform 61×31 mesh is used for computing lower-Ra cases and an 81×41 mesh for higher-Ra cases.

Table I. Effect of grid mesh size on mean Nusselt number $\overline{Nu}$ of a concentric rotational annulus ($Ra = 10^6$, $Re = 1000$, $\varepsilon = 0$, $RR = 2.6$, $Pr = 0.7$)

Grid size	41×31	61×31	81×41	91×61
$\overline{Nu}$	5.526	5.483	5.472	5.466

The validity of the numerical model is tested on the experimental natural convection in a stationary concentric annulus. In Figure 3 the present results of local Nusselt number distribution at $Ra = 4.7 \times 10^4$, $Pr = 0.706$ and $RR = 2.6$ for the inner and outer cylinders show good agreement with the experimental data of Kuehn and Goldstein [22]. Since there are no experimental data or theoretical solutions available for the case of a rotating inner cylinder with eccentric geometry, we compare our results against the numerical solution of Lee [9] to validate the present model. Figure 4 shows that the mean Nusselt numbers obtained in the present paper are in good agreement with those obtained by Lee [9].

Figure 5(a) depicts the streamlines and isotherms in a concentric annulus for various Rayleigh numbers with fixed $Re = 1000$, $RR = 2.6$ and $Pr = 0.7$. As seen from these contours, when Ra increases, the basic structures of the flow field and temperature field show the following features: (i) a rise of the buoyant plume towards the top of the outer cylinder; (ii) an increase in the thickness of the thermal boundary layer along the inner cylinder; (iii) more distorted contours of streamlines and isotherms in the annulus gap. These features indicate that a higher Rayleigh number can increase the strength of the recirculation, as proved by the increasing values of the maximum streamfunction Ψ_m and its location moving further upwards. The isotherms become closer as Ra increases, indicating large temperature gradients with a higher local heat transfer coefficient. The local Nusselt number (Nu) distribution is illustrated in Figure 5(b). The variations in Nu become more uniform and monotonic as Ra decreases. This is because, as Ra decreases, the rotation effect gradually becomes stronger than

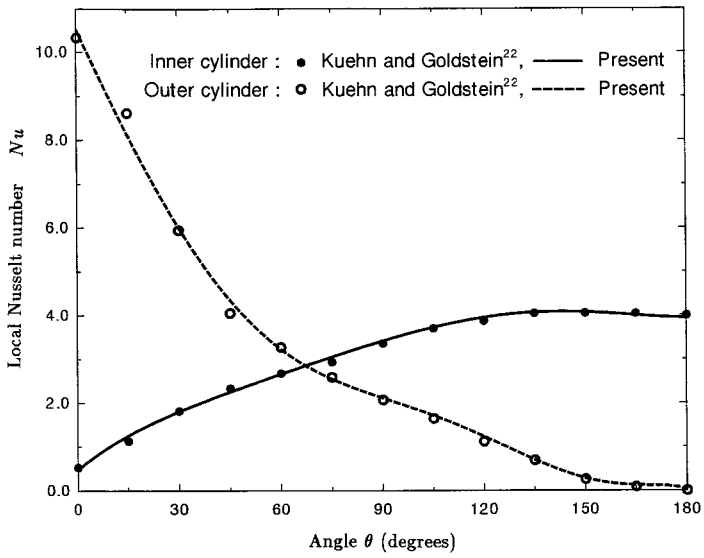

Figure 3. Distribution of Nu for inner and outer cylinders at $Ra = 4.7 \times 10^4$, $Re = 0$, $\varepsilon = 0$ and $Pr = 0.706$; comparison with experimental results of Kuehn and Goldstein [22]

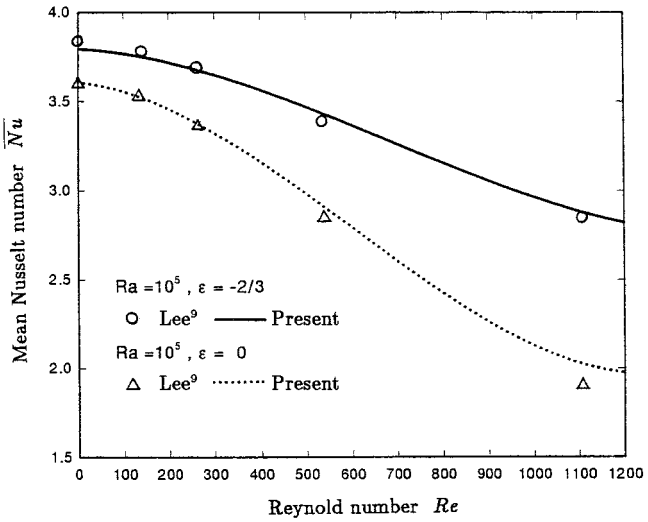

Figure 4. Variation of $\overline{Nu}$ with Re for various ε ($Ra = 10^5$, $RR = 2.6$, $Pr = 0.7$); comparison with numerical results of Lee [9]

the buoyancy effect. When Ra increases, both the maximum local heat flux on the outer cylinder and the minimum local heat flux on the inner cylinder are increased and moved to the mid-line ($\theta = 0$) in the annulus, demonstrating that the effect of the buoyant convection is larger than that of the centrifugally forced convection. For example, the point of minimum heat flux on the inner cylinder is moved to $\theta = -39°$ with $Nu_i = 2.92$ and $\theta = -99°$ with $Nu_i = 1.77$ at $Ra = 7 \times 10^6$ and 7×10^5 respectively.

Figure 6(a) shows the streamlines and isotherms in a stationary eccentric annulus with $Re = 0$, $RR = 2.6$ and $Ra = 10^5$ ($\sigma = \infty$) at eccentricities $\varepsilon = -0.8$, 0 and 0.8. The streamline and isotherm contours are symmetric with respect to the mid-line ($\theta = 0$), with one convective cell on either side of the vertical co-ordinate. The flow and temperature distributions in the eccentric cases are significantly different from those in the corresponding concentric cases. As the inner cylinder is moved upwards ($\varepsilon > 0$), the flow-induced thermal stratification below the inner cylinder increases, leading to a reduction in flow strength. This is clearly seen from the Ψ_m-values given in Figure 6(a). The thermally stratified field for $\varepsilon > 0$ is clearly evident in isotherm patterns such as Figure 6(a) (a). However, when the inner cylinder is moved downwards ($\varepsilon < 0$), flow-induced thermal stratification in the primary flow area above the inner cylinder does not occur. This is due to the fact that under negative eccentricity conditions the fluid has more sufficiently open space above the inner cylinder for convection than under positive eccentricity conditions. The vortex becomes stronger with increasing Ψ_m. Figure 6(b) shows the distributions of local Nusselt number around the outer and inner cylinders for various eccentricities. It can be seen from Figure 6(b) that the location of the peak value always occurs along the mid-line. When $\varepsilon = 0.8$, owing to insufficient space for buoyancy-induced flow to develop, a two-peak phenomenon can be found in this configuration.

The mean Nusselt number $\overline{Nu}$ has been plotted against Ra in Figures 7 and 8 for various eccentricities with $Re = 1000$, $Pr = 0.7$ and $RR = 2.6$. As Ra increases, the mean Nusselt number $\overline{Nu}$ increases considerably because of the stronger convective flow at higher Rayleigh numbers. At lower Ra ($\leq 1.4 \times 10^5$), where thermal stratification is not important, negative or positive ε results in an increase in overall heat transfer. At higher Ra ($\geq 7 \times 10^5$), flow-induced

thermal stratification effects in the lower half of the annulus are promoted. With positive ε, thermal stratification in the lower half of the annulus increases, leading to retardation and reduction of heat transfer. The opposite effect occurs at negative ε and causes a stronger convective flow and greater heat transfer. The buoyancy-driven flow is more vigorous in negative eccentricities. Another conclusion which can be drawn from Figure 8 is that the optimal location where minimum mean heat transfer occurs is strongly affected by the eccentricity. When ε increases (inner cylinder moving upwards), the eccentricity causes a significant reduction in mean heat transfer at higher *Ra*. However, adverse effects due to

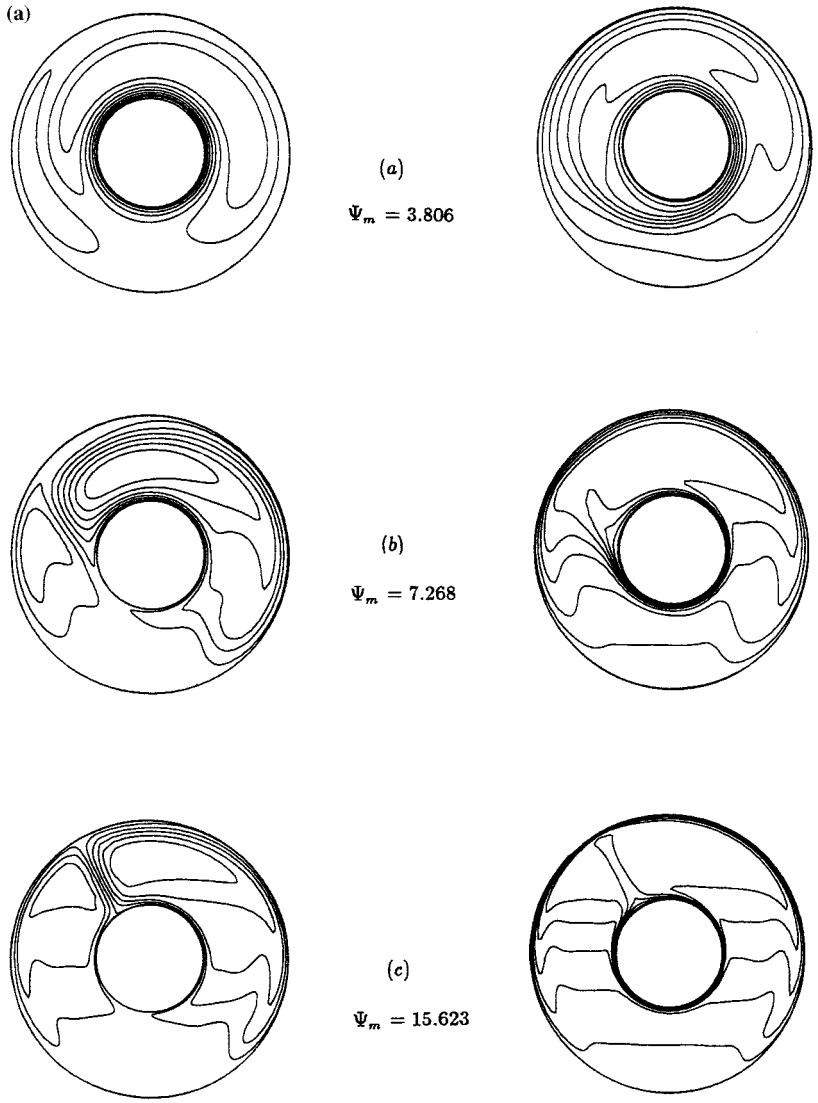

Figure 5. (a) Streamlines and isotherms at $Re = 1000$, $\varepsilon = 0$, $RR = 2.6$, and $Pr = 0.7$: (*a*) $Ra = 7 \times 10^4$ ($\sigma = 0.1$); (*b*) $Ra = 7 \times 10^5$ ($\sigma = 1$); (*c*) $Ra = 7 \times 10^6$ ($\sigma = 10$); (b) circumferential variation of *Nu* for various *Ra* at $Re = 1000$, $\varepsilon = 0$, $RR = 2.6$ and $Pr = 0.7$: $Ra = 7 \times 10^6$ ($\sigma = 10$); $Ra = 3.5 \times 10^6$ ($\sigma = 5$); $Ra = 1.4 \times 10^6$ ($\sigma = 2$); $Ra = 7 \times 10^5$ ($\sigma = 1$); $Ra = 7 \times 10^4$ ($\sigma = 0.1$)

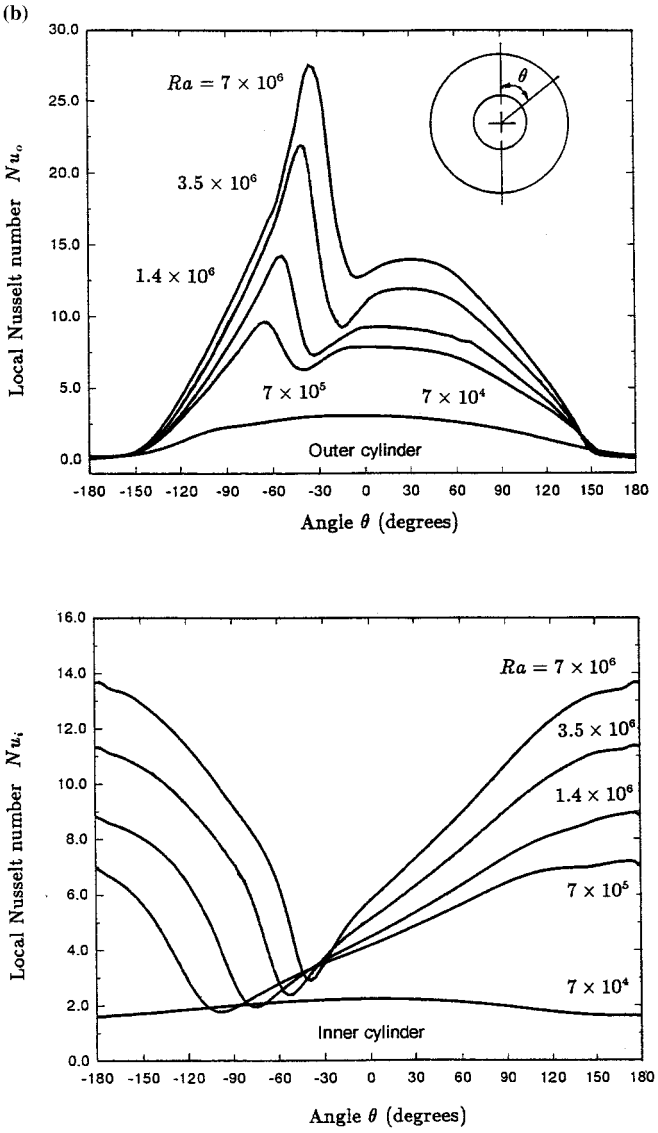

Figure 5 (*Continued*)

eccentricity can be found in lower-Ra cases. This indicates that the pure conduction effect cannot be neglected in the narrow throat gap. For example, the optimal location occurs at $\varepsilon = 0, \ -0.8$ with $Ra = 7 \times 10^3$ and 7×10^5 respectively.

Furthermore, in the Ra regime $7 \times 10^3 \leq Ra \leq 10^7$, convection effects are evidently important for various eccentricities ε at $Re = 1000$, $Pr = 0.7$ and $RR = 2.6$. By means of least-squares regression analysis the present results of mean Nusselt number can be correlated by the respective expressions

$$\overline{Nu} = 0.143 \times Ra^{0.252} \times \exp(0.66\varepsilon^2 - 0.26\varepsilon), \quad \varepsilon \geq 0, \tag{35}$$

$$\overline{Nu} = 0.172 \times Ra^{0.242} \times \exp(0.74\varepsilon^2 + 0.17\varepsilon), \quad \varepsilon < 0. \tag{36}$$

These correlations predict mean Nusselt numbers within 12% of the numerically obtained values.

The effects of rotation of the inner cylinder are studied through the variation of *Re*. Figure 9(a) shows the streamlines and isotherms in a concentric annulus with fixed $Ra = 10^5$ at various rotational Reynolds numbers. As seen from these contours, when *Re* increases, the basic structures of the flow field show the following features: (i) predominant growth of the right-hand cell; (ii) the number of rings of streamlines appearing around the inner cylinder increases; (iii) the rise of the thermal plume tends to the descending side; (iv) the thickness of the thermal boundary layer along the inner cylinder decreases; (v) there are more monotonic and asymmetric contours in the annulus gap. These features indicate that a higher Reynolds

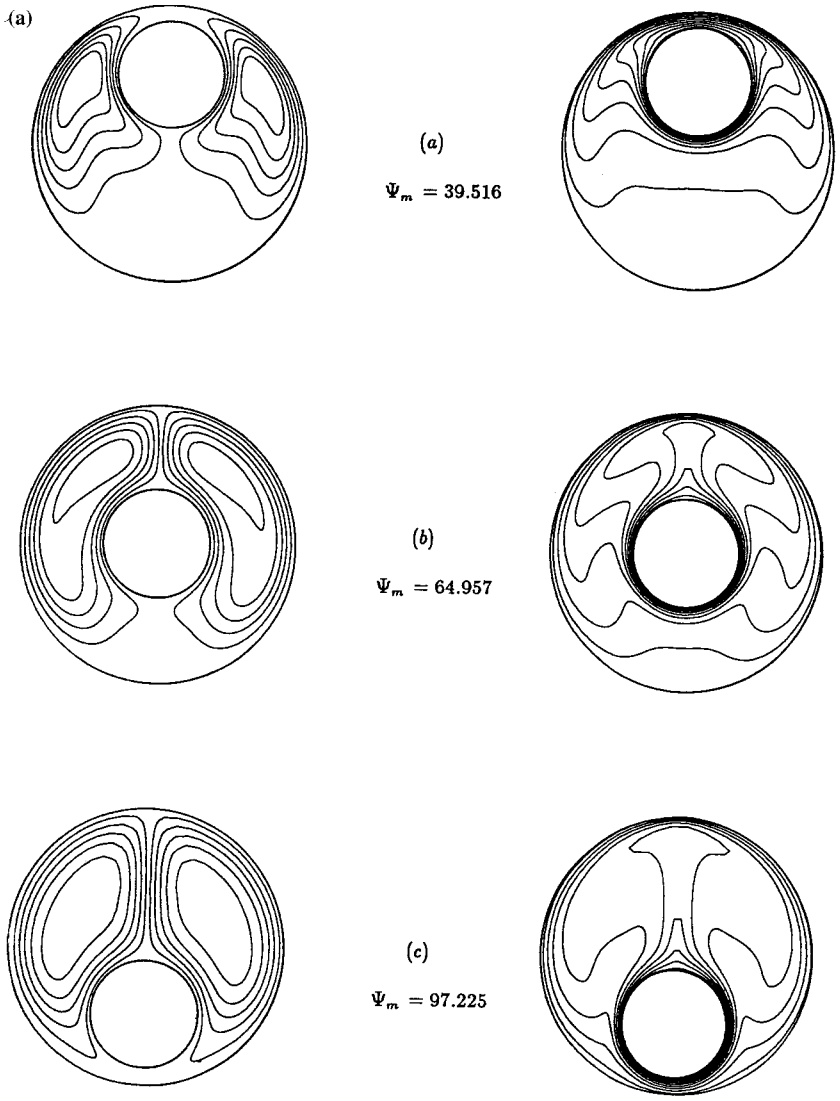

Figure 6. (a) Streamlines and isotherms at $Ra = 10^5$, $Re = 0$ ($\sigma = \infty$), $RR = 2.6$ and $Pr = 0.7$: (*a*) $\varepsilon = 0.8$; (*b*) $\varepsilon = 0$; (*c*) $\varepsilon = -0.8$; (b) circumferential variation of *Nu* for various ε at $Ra = 10^5$, $Re = 0$ ($\sigma = \infty$), $RR = 2.6$ and $Pr = 0.7$

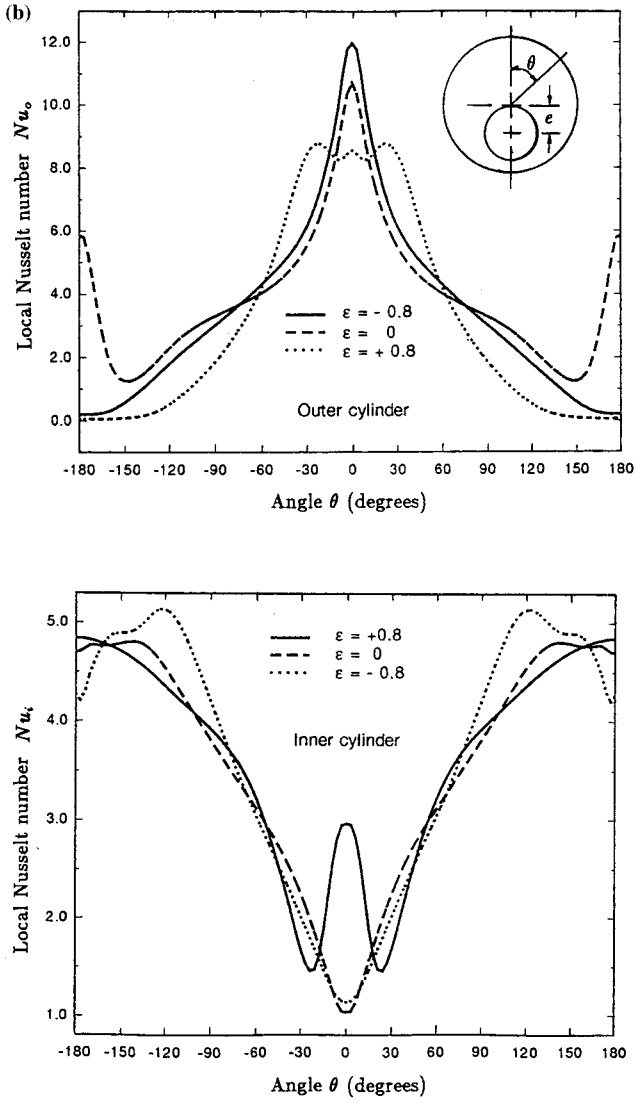

Figure 6 (*Continued*)

number can reduce the strength of the secondary flow, as evidenced by the decreasing values of the maximum streamfunction Ψ_m and the moving of its location to the descending side. The isotherms become looser, which indicates a smaller temperature gradient. The effects of rotation on the local Nusselt number *Nu* are illustrated in Figure 9(b). When *Re* increases, the location of maximum local heat flux on the outer cylinder moves to the descending side and the peak value of the local Nusselt number is reduced. The point of minimum local heat flux on the inner cylinder, which corresponds to the location of the root of the thermal plume, also moves in the same way. As *Re* increases from 0 to 1195, which is equivalent to σ decreasing from ∞ (pure natural convection) to 0.1, the areas under the local heat flux curves on both cylinders become smaller. This indicates that the distributions of local heat transfer on the cylinders become more uniform as *Re* is increased.

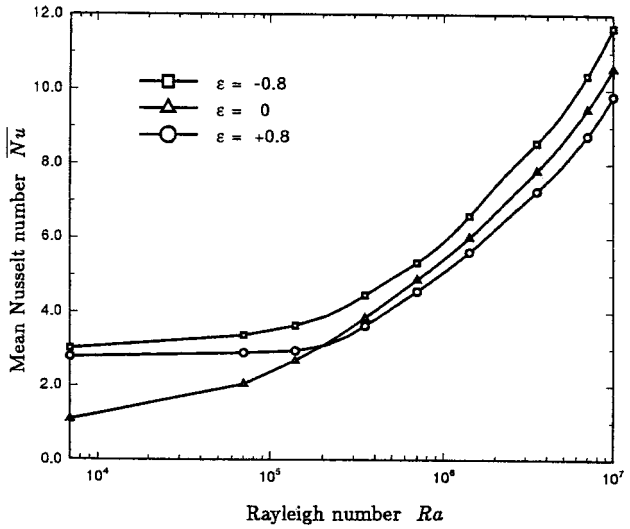

Figure 7. Effect of Ra on $\overline{Nu}$ for various ε at $Re = 1000$, $RR = 2.6$ and $Pr = 0.7$

Figures 10 and 11 show the variation in $\overline{Nu}$ with fixed $Ra = 10^5$, $RR = 2.6$ and $Pr = 0.7$ for various eccentricities and Reynolds numbers. In general, the more Re increases, the more the mean Nusselt number $\overline{Nu}$ decreases, except at larger positive eccentricities ($\varepsilon > 0.6$). This special phenomenon can be explained as the effect of increasing pure conduction overcoming the effect of decreasing mixed convection, resulting in heat conduction becoming predominant in the narrowest throat gap, which is apparent from the isotherm plots. In this paper it is important to find the optimal location where minimum mean heat transfer occurs. When ε increases (inner cylinder moving upwards) from -0.8 to 0.8, the space of the convective region is reduced, causing a decrease in $\overline{Nu}$. However, adverse effects can be found with

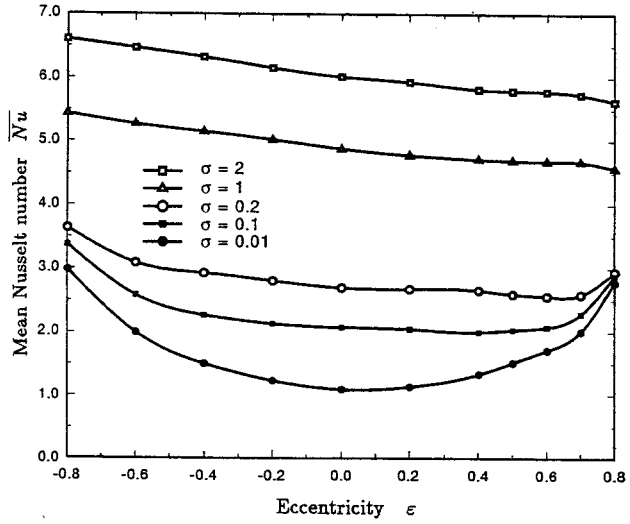

Figure 8. Effect of ε and Ra on $\overline{Nu}$ at $Re = 1000$, $RR = 2.6$, and $Pr = 0.7$: $Ra = 1.4 \times 10^6$ ($\sigma = 2$); $Ra = 7 \times 10^5$ ($\sigma = 1$); $Ra = 1.4 \times 10^5$ ($\sigma = 0.2$); $Ra = 7 \times 10^4$ ($\sigma = 0.1$); $Ra = 7 \times 10^3$ ($\sigma = 0.01$)

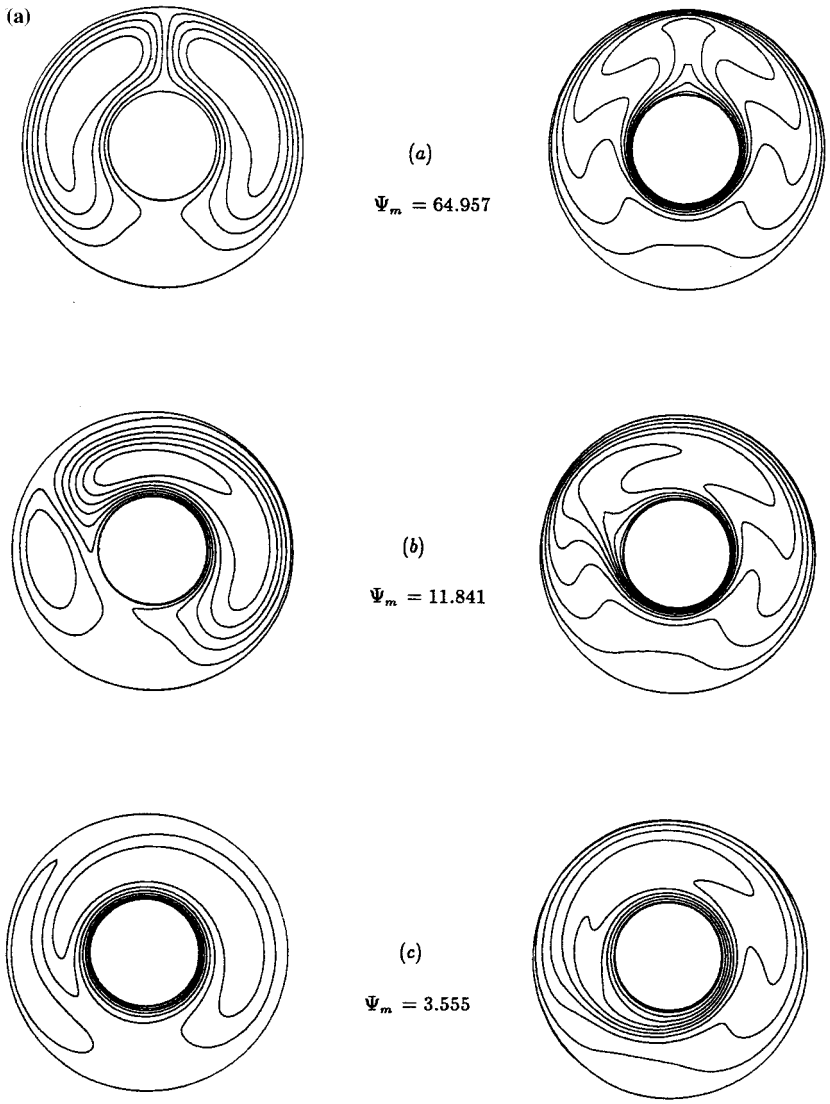

Figure 9. (a) Streamlines and isotherms at $Ra = 10^5$, $\varepsilon = 0$, $RR = 2.6$ and $Pr = 0.7$: (*a*) $Re = 0$ ($\sigma = \infty$); (*b*) $Re = 378$ ($\sigma = 1$); (*c*) $Re = 1195$ ($\sigma = 0.1$); (b) circumferential variation of Nu for various Re at $Ra = 10^5$, $\varepsilon = 0$, $RR = 2.6$, and $Pr = 0.7$: $Re = 0$ ($\sigma = \infty$); $Re = 119$ ($\sigma = 10$); $Re = 378$ ($\sigma = 1$); $Re = 1195$ ($\sigma = 0.1$)

stronger rotation at higher positive eccentricities ($\varepsilon > 0.6$). As noted earlier, this indicates that the pure conduction effect cannot be neglected in the narrow throat gap. For example, at fixed $Ra = 10^5$ the optimal location for heat transfer occurs at $\varepsilon = 0$ and -0.7 with $Re = 0$ ($\sigma = \infty$) and $Re = 1195$ ($\sigma = 0.1$) respectively. For fixed $Ra = 10^5$, $Pr = 0.7$ and $RR = 2.6$ the eccentricity effects are extremely important to heat transfer in the rotational configuration ($Re > 0$). The correlations obtained from the numerical results in the present case are

$$\overline{Nu} = 4.31 \times Re^{-0.07} \times \exp(0.66\varepsilon^2 - 0.44\varepsilon), \quad \varepsilon \geq 0, \tag{37}$$

$$\overline{Nu} = 6.78 \times Re^{-0.13} \times \exp(0.68\varepsilon^2 + 0.31\varepsilon), \quad \varepsilon < 0. \tag{38}$$

These correlations predict mean Nusselt numbers within 11% of the correlated data.

Figure 12 displays the streamlines and isotherms for the concentric cases in which $Ra = 10^6$, $Re = 1000$ and $RR = 2.6$ with Prandtl numbers $Pr = 0.1$, 0.7 and 7. It shows clearly that the strength of the mixed convection increases as the Prandtl number increases, owing to the smaller mixed rotation parameter σ ($= Ra/PrRe^2$) for higher-Prandtl-number fluids. Hence the locations of Ψ_m and the thermal plume are moved to the descending side. Comparison of the isotherms indicates there exists a thinner thermal boundary layer along both surfaces in higher-Prandtl-number cases, owing to the effect that the thermal boundary layer is more confined around the inner and outer cylinders. Hence the temperature gradients along the inner and outer cylinders increase as the Prandtl number increases. Figure 13 shows the effect

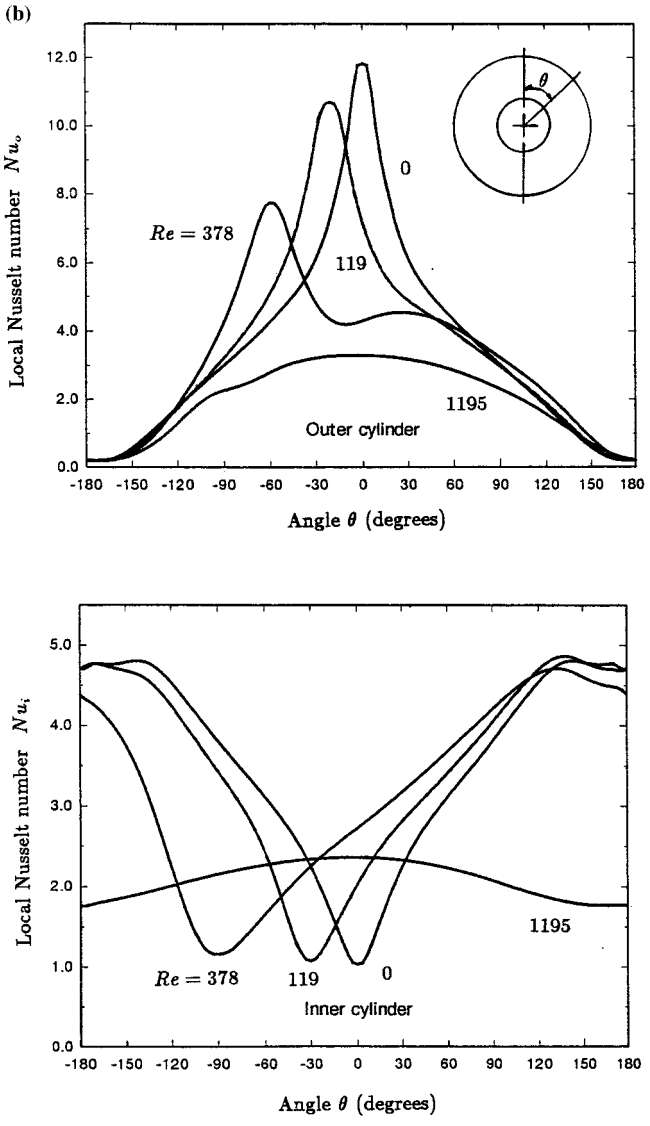

Figure 9 (*Continued*)

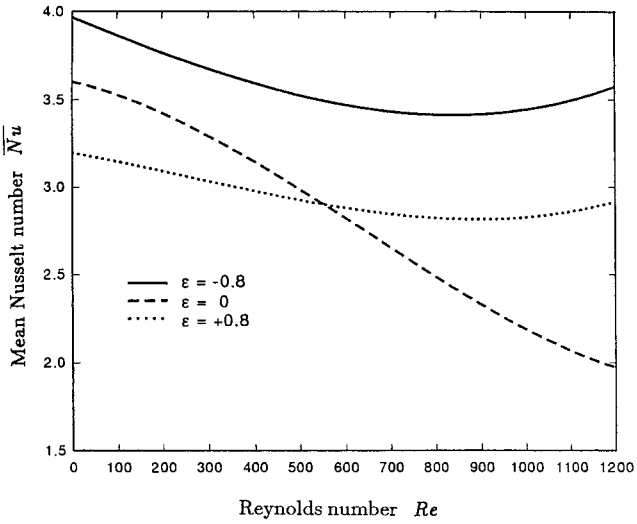

Figure 10. Effect of Re on $\overline{Nu}$ for various ε at $Ra = 10^5$, $RR = 2.6$ and $Pr = 0.7$

of the eccentricity ε on $\overline{Nu}$ for various Prandtl numbers with $Ra = 10^6$, $Re = 1000$ and $RR = 2.6$. It is observed from Figure 13 that the effect of changes in ε on the mean Nusselt number $\overline{Nu}$ is more pronounced for $Pr = 7$. Under this circumstance the mean Nusselt number $\overline{Nu}$ first decreases and then increases with increasing eccentricity. However, this trend is rather insensitive to changes in ε for the smaller Prandtl numbers $Pr = 0.01$, 0.1 and 0.7.

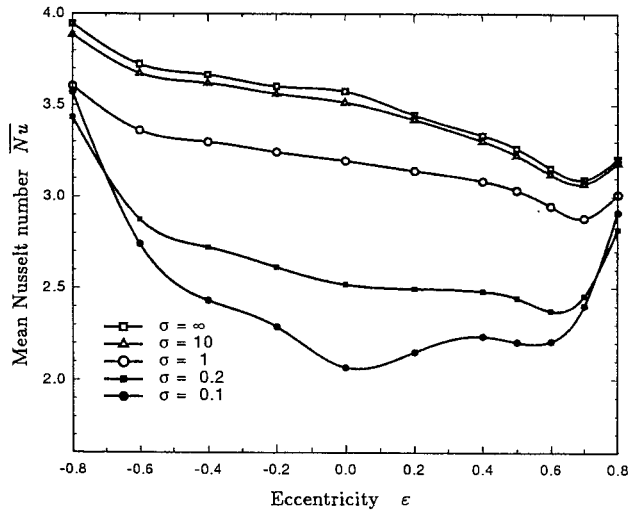

Figure 11. Effect of ε and Re on $\overline{Nu}$ at $Ra = 10^5$, $RR = 2.6$ and $Pr = 0.7$: $Re = 0$ ($\sigma = \infty$); $Re = 119$ ($\sigma = 10$); $Re = 378$ ($\sigma = 1$); $Re = 845$ ($\sigma = 0.2$); $Re = 1195$ ($\sigma = 0.1$)

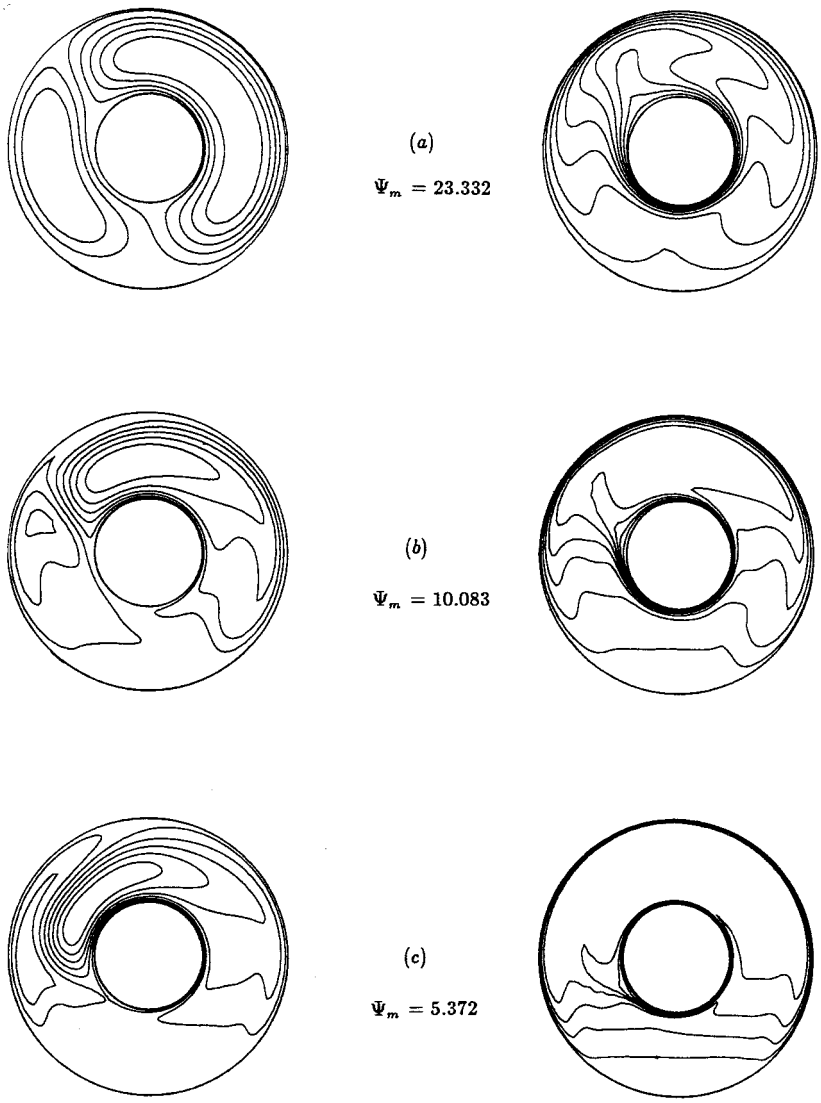

Figure 12. Streamlines and isotherms at $Ra = 10^6$, $Re = 1000$, $\varepsilon = 0$ and $RR = 2.6$: (*a*) $Pr = 0.1$ ($\sigma = 10$); (*b*) $Pr = 0.7$ ($\sigma = 1.43$); (*c*) $Pr = 7$ ($\sigma = 0.143$)

5. CONCLUDING REMARKS

A numerical simulation has been performed for the problem of mixed convection in an annulus between two eccentric horizontal cylinders with a heated rotating inner cylinder. The governing equations in the computational domain were solved numerically by a finite volume formulation using the non-orthogonal, fully collocated code STREAM. The convection is represented by the MUSCL scheme and solutions are iterated to convergence through pressure correction. The numerical procedure adopted in this study can easily eliminate the 'numerical leakage' phenomenon encountered in the mixed convection problem in a highly eccentric annulus. The numerical solutions are in good agreement with published results. The following conclusions can be drawn from the present study.

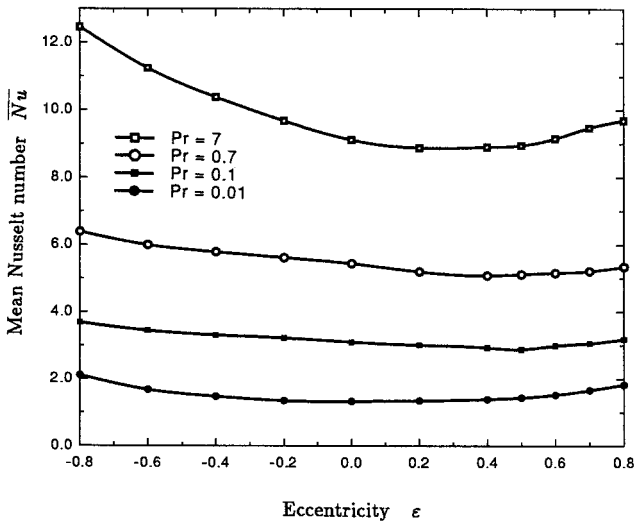

Figure 13. Effect of ε and Pr on $\overline{Nu}$ at $Ra = 10^6$, $Re = 1000$ and $RR = 2.6$

1. For fixed Re and Pr, thermal stratification is not important: negative or positive ε causes an increase in overall heat transfer at lower σ (≤ 0.2). With a larger mixed rotation parameter σ (≥ 1), flow-induced thermal stratification effects in the lower half of the annulus are promoted. With positive ε, thermal stratification in the lower half increases, leading to retardation and reduction of heat transfer. The opposite effect occurs at negative ε, causing a stronger convective flow and greater heat transfer.
2. For all configurations, the larger the mixed rotation parameter σ is, the greater the maximum streamfunctions Ψ_m becomes. When σ decreases in the concentric annulus, the locations of the thermal plume and the maximum streamfunction Ψ_m are moved to the descending side, corresponding to the maximum and minimum values of local Nusselt number around the outer and inner cylinders respectively.
3. For fixed σ (mixed rotation parameter), when the eccentricity ε increases, i.e. the inner cylinder moves upwards along the mid-line ($\theta = 0$), the value of the maximum streamfunction Ψ_m decreases and the location of the thermal plume moves to the descending side, except for $\sigma = \infty$ (pure natural convection).
4. The mean Nusselt number $\overline{Nu}$ is significantly affected by the eccentricity ε, especially for small σ at large eccentricities. When ε increases, the mean Nusselt number $\overline{Nu}$ first decreases and then increases.
5. The optimal location where minimum heat transfer occurs is affected by σ and ε. When σ increases, the optimal location shifts upwards in the annulus, while for small σ the optimal location occurs at the middle of the annulus.

APPENDIX A. NOMENCLATURE

e	distance between axes of inner and outer cylinders of eccentric annulus
g	gravitational acceleration
J	Jacobian of co-ordinate transformation
L	characteristic length

n	normal vector on wall
Nu, $\overline{Nu}$	local and mean Nusselt numbers
O, O′	centres of outer and inner cylinders
p, P	dimensional and dimensionless pressures
Pr	Prandtl number
r	radial co-ordinate
Ra	Rayleigh number
Re	Reynolds number of inner cylinder
RR	radius ratio ($=R_o/R_i$)
R_i, R_o	inner and outer cylinder radii
R_m	mass imbalance
R_u	residue value
S_C	explicit part of source term
S_P	implicit part of source term
S_ϕ	source term pertaining to scalar variable ϕ
S^{CD}	source term pertaining to cross-diffusion
T_i, T_o	temperatures of inner and outer cylinders
T_m	reference temperature
u, U	dimensional and dimensionless velocities in X-direction
$\bar{U}$, $\bar{V}$	contravariant velocities
v, V	dimensional and dimensionless velocities in Y-direction
x, X	dimensional and dimensionless co-ordinates in horizontal direction
y, Y	dimensional and dimensionless co-ordinates in vertical direction
Z	number of grid cells

Greek letters

α	thermal diffusivity
α_p	underrelaxation factor for pressure P'
β	coefficient of volumetric expansion
ε	eccentricity
θ	azimuthal angle measured from positive Y-axis
Θ	dimensionless temperature
μ	dynamic viscosity
ν	kinematic viscosity
ξ, η	dimensionless transformed co-ordinates
ρ	density
σ	mixed rotation parameters ($=Ra/PrRe^2$)
ϕ	scalar property
Ψ	streamfunction
ω	rotating speed of inner cylinder

Superscripts

$(^-)$	time averaging
$(\,)'$	correction or perturbation
$(\,)^*$	provisional field

Subscripts

e, w, n, s	east, west, north and south faces of control volume
P, E, W, N, S	centre of control volume and surrounding nodes in east, west, north and south directions

REFERENCES

1. H.Q. Yang, 'Diffusion-controlled mass transfer from a rotating cylinder', *Numer. Heat Transfer A*, **23**, 303–318 (1993).
2. K.T. Yang, H.Q. Yang and J.R. Lloyd, 'Rotational effects on natural convection in a horizontal cylinder', *AIChE J.*, **34**, 1627–1633 (1988).
3. M. Prudhomme and L. Robillard, 'Natural convection in an annular fluid layer rotating at weak angular velocity', *Proc. 4th Int. Symp. on Transport Phenomena, Heat and Mass Transfer*, Sydney, N.S.W., 1991, p. 38.
4. C.P. Desai and K. Vafai, 'An investigation and comparative analysis of two- and three-dimensional turbulent natural convection in a horizontal annulus', *Int. J. Heat Mass Transfer*, **37**, 2475–2504 (1994).
5. C.K. Chen, S.W. Hsiao and P. Cheng, 'Transient natural convection in an eccentric porous annulus between horizontal cylinders', *Numer. Heat Transfer A*, **17**, 431–448 (1990).
6. J. Prusa and L.S. Yao, 'Natural convection heat transfer between eccentric horizontal cylinder', *J. Heat Transfer*, **105**, 108–116 (1983).
7. E.E. Feldman, R.R. Hornbeck and J.F. Osterle, 'A numerical solution of laminar developing flow in eccentric annular ducts', *Int. J. Heat Mass Transfer*, **25**, 231–241 (1982).
8. E.E. Feldman, R.W. Hornbeck and J.F. Osterle, 'A numerical solution of developing temperature for laminar developing flow in eccentric annular ducts', *Int. J. Heat Mass Transfer*, **25**, 243–253 (1982).
9. T.S. Lee, 'Numerical computation of fluid convection with air enclosed between the annuli of eccentric heated horizontal rotating cylinders', *Comput. Fluids*, **21**, 355–368 (1992).
10. D. Choudhury and K.C. Karki, 'Laminar mixed convection in a horizontal eccentric annulus', *Numer. Heat Transfer A*, **22**, 87–108 (1992).
11. S.R.M. Gardiner and R.H. Sabersky, 'Heat transfer in annular gap', *Int. J. Heat Mass Transfer*, **21**, 1459–1466 (1978).
12. G. Guj, S. Iannetta and G. Moretti, 'Experimental analysis of thermal fields in horizontally eccentric cylindrical annuli', *Exp. Fluids*, **12**, 385–393 (1992).
13. C.J. Ho and F.J. Tu, 'Laminar mixed convection of cold water in a vertical annulus with a heated rotating inner cylinder', *J. Heat Transfer*, **114**, 418–424 (1992).
14. T. Fusegi, B. Farouk and S.B. Kenneth, 'Mixed convection flows within a horizontal concentric annulus with a heated rotating inner cylinder', *Numer. Heat Transfer*, **9**, 591–604 (1986).
15. Z.Y. Guo and C.M. Zhang, 'Thermal drive in centrifugal fields mixed convection in a vertical rotating cylinder', *Int. J. Heat Mass Transfer*, **35**, 1635–1644 (1992).
16. F.S. Lien and M.A. Leschziner, 'A general non-orthogonal finite volume collocated algorithm for turbulent flow at all speeds incorporating second-moment turbulence-transport closure, Part 1: Computational implementation, Part 2: Application', *Comput. Meth. Appl. Mech. Engng.*, **114**, 123–167 (1993).
17. Y.N. Jeng and J.L. Chen, 'Geometric conservation law of the finite-volume method for the simpler algorithm and a proposed upwind scheme', *Numer. Heat Transfer B*, **22**, 211–234 (1992).
18. E.H. Chui and G.D. Raithby, 'Computation of radiant heat transfer on a non-orthogonal mesh using the finite-volume method', *Numer. Heat Transfer B*, **23**, 269–288 (1993).
19. B. van Leer, 'Towards the ultimate conservation difference scheme V, A second-order sequel to Godunov's method', *J. Comput. Phys.*, **32**, 101–136 (1979).
20. C.M. Rhie and W.L. Chow, 'Numerical study of the turbulent flow past an airfoil with trailing edge separation', *AIAA J.*, **21**, 1525–1532 (1983).
21. S.V. Patankar, *Numerical Heat Transfer and Fluid Flow*, Hemisphere, Washington, DC, 1980.
22. T.H. Kuehn and R.J. Goldstein, 'An experimental study of natural convection heat transfer in concentric and eccentric horizontal cylindrical annuli', *J. Heat Transfer*, **100**, 635–640 (1978).

